Brain Multiphysics 2 (2021) 100035

Contents lists available at ScienceDirect

Brain Multiphysics

journal homepage: www.sciencedirect.com/journal/brain-multiphysics

Hyperelastic material properties of axonal fibers in brain white matter

Poorya Chavoshnejad [a], Guy K. German [b,c], Mir Jalil Razavi [a,*]

[a] Department of Mechanical Engineering, Binghamton University, State University of New York, Binghamton, NY 13902, USA
[b] Department of Biomedical Engineering, Binghamton University, State University of New York, Binghamton, NY, 13902, USA
[c] Department of Pharmaceutical Sciences, Binghamton University, State University of New York, Binghamton, NY, 13902, USA

ARTICLE INFO

Keywords:
Axon
White matter
Material properties
Hyperelastic
Finite element method

ABSTRACT

Accurate characterization of the mechanical properties of the human brain at both microscopic and macroscopic length scales is a critical requirement for modeling of traumatic brain injury and brain folding. To date, most experimental studies that employ classical tension/compression/shear tests report the mechanical properties of the brain averaged over both the gray and white matter within the macroscopic regions of interest. As a result, there is a missing correlation between the independent mechanical properties of the microscopic constituent elements and the composite bulk macroscopic mechanical properties of the tissue. This microstructural computational study aims to inversely predict the hyperelastic mechanical properties of the axonal fibers and their surrounding extracellular matrix (ECM) from the bulk tissue's mechanical properties. We develop a representative volume element (RVE) model of the bulk tissue consisting of axonal fibers and ECM with the embedded element technique. A multiobjective optimization technique is implemented to calibrate the model and establish the independent mechanical properties of axonal fibers and ECM based on seven previously reported experimental mechanical tests for bulk white matter tissue from the corpus callosum. The result of the study shows that the discrepancy between the reported values for the elastic behavior of white matter in literature stems from the anisotropy of the tissue at the microscale. The shear modulus of the axonal fiber is seven times larger than the ECM, with axonal fibers that also show greater nonlinearity, contrary to the common assumption that both components exhibit identical nonlinear characteristics.

STATEMENT OF SIGNIFICANCE

The reported mechanical properties of white matter microstructure used in traumatic brain injury or brain mechanics studies vary widely, in some cases by up to two orders of magnitude. Currently, the material parameters of the white matter microstructure are identified by a single loading mode or ultimately two modes of the bulk tissue. The presented material models only define the response of the bulk and homogenized white matter at a macroscopic scale and cannot explicitly capture the connection between the material properties of microstructure and bulk structure. To fill this knowledge gap, our study characterizes the hyperelastic material properties of axonal fibers and ECM using microscale computational modeling and multiobjective optimization. The hyperelastic material properties for axonal fibers and ECM presented in this study are more accurate than previously proposed because they have been optimized using seven or six loading modes of the bulk tissue, which were previously limited to only two of the seven possible loading modes. As such, the predicted values with high accuracy could be used in various computational modeling studies. The systematic characterization of the material properties of the human brain tissue at both macro- and microscales will lead to more accurate computational predictions, which will enable a better understanding of injury criteria, and has a positive impact on the improved development of smart protection systems, and more accurate prediction of brain development and disease progression.

* Corresponding author.
E-mail address: mrazavi@binghamton.edu (M.J. Razavi).

https://doi.org/10.1016/j.brain.2021.100035
Received 14 July 2021; Received in revised form 21 September 2021; Accepted 22 September 2021
Available online 2 October 2021

1. Introduction

The human brain is divided into two distinct layers: the thin superficial gray matter and the larger core white matter. Gray matter consists primarily of neuronal cell bodies, while white matter is comprised of axonal fibers covered with myelin sheaths [1]. Mechanical testing of brain tissue, in gray or white matter, is a challenging task due to its high mechanical compliance and complex composition. As a result, most experimental studies report controversial and diverse mechanical properties for the human brain at both global macroscopic and smaller localized length scales [2–7]. Human brain tissue shows a highly nonlinear and viscoelastic mechanical response [91] with a noticeable compression-tension asymmetry [2, 8, 9]. Therefore, material parameters identified for a single loading mode cannot be used to accurately predict the realistic mechanical response under multiaxial loading. The study of the mechanical behavior of white matter is more difficult than studies of gray matter because the tissue exhibits structural and mechanical anisotropy [10]. This is attributable to the presence of stiff myelinated axonal fibers embedded within the soft ground substance (extracellular matrix) [11–13]. These fibers are clearly visible in a sample electron micrograph of murine corpus callosum (CC) in Fig. 1. Axons are cross-linked by microtubule associated proteins [14]. The diameter and length of these microtubule bundles can reach several orders of magnitude [15, 16]. Myelin is a lipid-rich substance whose dry mass is composed of 70-85% lipids and 15-30% protein [17]. Its purpose is to insulate electrical signal propagation and improve electrical function [18]. Brain stiffness is related to its fundamental microstructure, in particular the local myelin content [19, 20]. Prior studies reveal that the density and diameters of axonal fibers vary with anatomical site in the CC and corona radiata [21–25]. These impact the localized mechanical behavior of the tissue [26].

Reported values for the relative stiffness ratio of axonal fibers to ground substance can vary greatly, with stiffness ratios of 1.8, 2, 3, 7, 10, and 11 previously disclosed for different applied strain ranges [11, 12, 28]. At small strains, this discrepancy is mainly attributed to the processing and preparation of samples, testing tools and methods, variances in regional/directional of brain tissues, and implemented computational models to predict the mechanical properties [7]. With the timely need to obtain more accurate mechanical properties of the brain for the improved modeling of brain trauma, brain folding, and tumor growth, models need to be compared with experimental data. As an available technique, magnetic resonance elastography (MRE) typically measures the average bulk mechanical properties of the whole brain and is not a sufficiently powerful tool to capture the directional dependency of the tissue. Axonal fibers are locally distributed and oriented in specific regions of the white matter; therefore, the induced stress, strain, and deformations fields are considerably anisotropic. This places MRE at a neurological diagnostic disadvantage because brain disorders are mostly localized or have disruptions in specific regions. Furthermore, there are occasional contradictions between reported results of the bulk mechanical stiffness of the brain, and regional variations in stiffness reported by MRE [29–35].

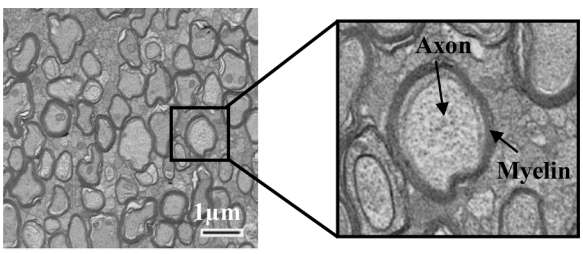

Fig. 1. Electron microscopy of corpus callosum. An axonal fiber includes an axon and a myelin sheath. Figure adopted and used by permission from Ref. [27].

A majority of prior white matter constitutive models assume isotropy or transverse-isotropy [12, 13, 36–38]. Isotropic hyperelastic material models, such as neo-Hookean, Ogden, Mooney-Rivlin, Hyperfoam, Polynomial, and Arruda-Boyce [2, 4, 5, 39], have also been proposed as well as anisotropic models [11, 40–43]. However, these models define only the mechanical response of the assumed bulk and homogenized white matter at a macroscopic scale and cannot explicitly capture the connection between the microstructural composition and the bulk anisotropic mechanical properties of the tissue. It has been shown that quantifying localized stress/strain or stiffness maps in the white matter are of great importance to many applications that include brain traumatic injury (TBI), diffusive axonal injuries (DAI), and neurodegenerative brain disorders [44–54]. Therefore, there has been a timely need to develop a more accurate mechanical model of the brain that can predict how the tissue structure governs the microstructural mechanics of the tissue. To date, this effort has been impeded by the lack of independent mechanical data of individual axonal fibers and ECM (i.e., glia and vasculature), primarily due to the small scale of the constituent elements and limitations of experimental tools and techniques that can evaluate these components [55]. In response to this need, contemporary micromechanical models have been developed that couple the heterogeneous microstructure of white matter with the macroscale bulk material behavior [56–64].

In micromechanical models, accurate characterization of axonal fiber and ECM mechanical properties is an essential component of correlating micro- and macroscale material responses. To date, most micromechanical modeling studies [56, 59, 60] have assumed that the axonal fibers are three times stiffer than the ECM, according to the provided data by Meaney [65]. However, more recently, a study that employed analytical and computational embedded element methods indicated that the axonal fibers are almost ten times stiffer than the ground substance under large deformations [62]. Results of this latter study shows a better agreement with experimental results [12]. Although these micromechanical modeling studies give valuable information regarding the micro- and macromechanics of brain white matter, results still vary widely; the stiffness ratios of axonal fiber to ECM vary between 1 and 11, greater than an order of magnitude in difference [11, 12, 28]. In all past micromechanical studies, an identical degree of nonlinearity has been assumed for the axon and ECM. This assumption is questionable because axonal fibers and ECM have substantial differences in their respective composition [18, 19, 66, 67]. Furthermore, the mechanical properties of the constituent materials have been extracted from only one or two loading modes of the bulk tissue. As the result, the accuracy and findings of the computational models of TBI or brain folding, which include axons or axonal fiber bundles, are likely to be limited [45, 68–70]. Therefore, there is a need to characterize the precise material behavior of axonal fibers and ECM in brain white matter on a comprehensive scale. To fill this knowledge gap, we construct an RVE model with an embedded element technique to uniquely determine the hyperelastic mechanical properties of the axonal fibers and the ECM. In doing so, we develop a multiobjective optimization process to calibrate the RVE and determine the independent mechanical properties of axonal fibers and the ECM based on the results of mechanical tests of white matter under seven loading modes.

2. Materials and methods

Micromechanical model

A micromechanical model is established that enables the mechanical behavior of the individual axonal fiber and ECM constituents to be inversely predicted from bulk mechanical testing of white matter. This is achieved through construction of a cubic three-dimensional RVE of CC, as shown in Fig. 2. In composite materials, RVE is the smallest volume in which its response is similar to the whole system [71–74]. The CC of white matter is selected as the region of interest because it has a tight

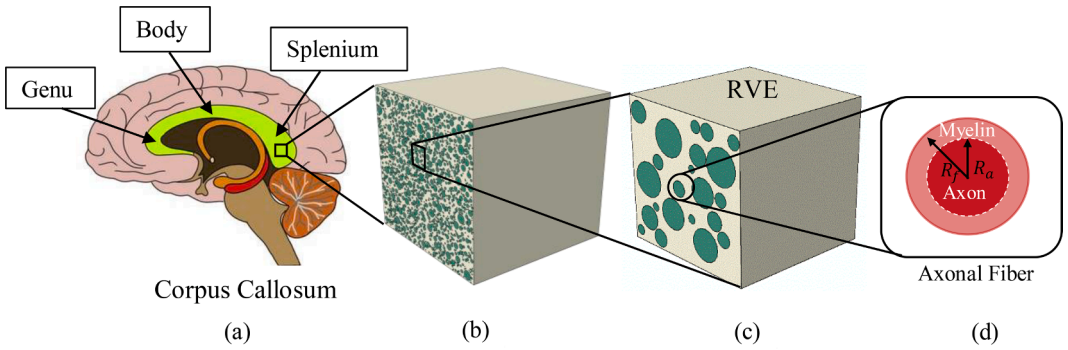

Fig. 2. (a) Corpus callosum of the human brain and its three major regions; Genu, Body, and Splenium. b) Three-dimensional cubic macromodel including soft matrix and aligned embedded axonal fibers. c) Three-dimensional RVE model with the randomly embedded axonal fibers and ECM. The circular cross-section of an axonal fiber includes the axon diameter and the myelin thickness. d) An axonal fiber consists of axon and myelin sheath. g ratio is defined as the ratio of the inner diameter of the axon to the outer diameter of the fiber: $g = R_a/R_f$.

Table 1
Mean value, standard deviation (SD), median, maximum and minimum value of axonal diameters (inner diameter of myelinated axons) in μm for different locations of CC. Permission to reprint this data has been granted from [25].

	Mean/SD	Median	Max	Min
Human Brain 1				
Genu	0.67±0.42	0.53	2.56	0.17
Body	0.67±0.44	0.53	3.16	0.19
Splenium	0.74±0.47	0.59	2.8	0.24
Human Brain 2				
Genu	0.73±0.45	0.58	2.43	0.19
Body	0.64±0.42	0.51	3.03	0.19
Splenium	0.7±0.56	0.51	5.13	0.18

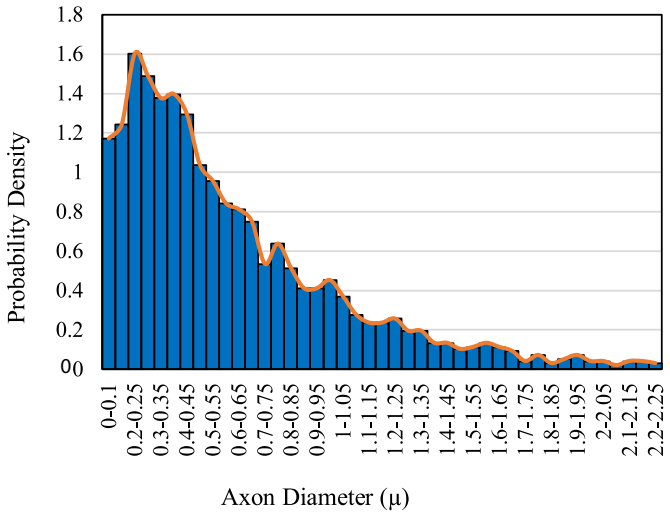

Fig. 3. The distribution of the axon fiber diameters from Table 1.

bundle of highly aligned axonal fibers. The unmodified homogeneous cubic model represents the ECM alone. Axonal fibers are then embedded into this RVE with a random distribution, as shown in Fig. 2(c). Due to the alignment of axonal fibers in the CC, embedded fibers are represented by straight cylinders with an axon radius, R_a, and myelin radius, R_f [56–60].

To generate an accurate RVE model, empirical distributions of axonal fiber diameters and volume fractions in the CC are required, which are extracted from previous reports [25]. In total, six sets of diameter and volume fraction distributions are used, with $n = 2$ independent measurements each from $n = 3$ locations in human CC: Genu, Body, and Splenium. Table 1 shows the average, standard deviation (SD), median, and maximum and minimum axonal fiber diameters (inner diameter of the myelinated axons) from the samples [25]. Fig. 3 shows the log-normal distribution of the axons' diameters based on an average of the six sets of data in Table 1.

Table 1 reports the outer diameter of axonal fibers. However, this length does not account for the surrounding myelin sheath. Several studies indicate that myelin has a significant effect on the overall composite mechanical properties of the white matter [19, 20]. To account for this increased thickness, we establish a g ratio in three different locations of the CC (genu, truncus, splenium), which denotes the ratio of the inner to the outer axon fiber diameter. The g ratios for genu, main body, and splenium are 0.55, 0.6, and 0.7, respectively [22]. These are employed to obtain the full axonal fiber diameters.

The Fiber volume fraction (FVF) is defined as the proportion of the whole tissue volume that is filled with axonal fibers:

$$FVF = \frac{\sum_1^N \pi {r_i}^2 L}{L^3} = \frac{\sum_1^N \pi {r_i}^2}{L^2} \tag{1}$$

where r_i is the i-th fiber radius (axon plus myelin), and L is the edge length for the cubic model. Because axonal fibers are aligned in only one direction, the FVF is reduced to the ratio of the total surface area occupied by the fibers to the surface area of the cube face. To obtain the correct FVF in the RVE, Fractional Anisotropy (FA) of the CC in the experimental work [2] is converted to FVF using the expression [22]

$$FVF = 0.883FA^2 - 0.082FA + 0.074 \tag{2}$$

For instance, Budday et al. [2] reported FA of 0.65 for CC. This results in an FVF close to 0.4, which indicates 40% of the CC is occupied by axonal fibers. Axonal fibers are sequentially embedded at random locations within the RVE as parallel cylinders orthogonal to the RVE face, which maintain a uniform cross-sectional area that extends to the opposite face. For simplification, fibers that cross RVE perimeter boundaries are removed and distributed again until the FVF reaches 40%. This simplification eliminates the need to apply a geometric periodic constraint on the edges of the RVE. The diameters of the embedded axonal fibers conform to the log-normal distribution presented in Fig. 3. To avoid overlap between fibers, a 0.05 μm threshold is assigned as the minimum acceptable distance between the outer diameters of two adjacent fibers. Both axonal fibers and ECM are meshed using a 10-node quadratic tetrahedron elements (C3D10H) in Abaqus finite element package [75]. C3D10H are hybrid elements and mostly intended for simulating incompressible materials. Optimum size of the RVE and mesh convergence are then studied. To investigate the reliability of the RVE, size and mesh independency studies were completed by varying the RVE edge length and mesh size. For this testing, all models were subjected to a 20% strain relative to the RVE edge length.

2.1.1. Periodic boundary condition

Periodic boundary conditions (PBC) are applied to the boundaries of the RVE that include all faces, edges and corners [76]. This ensures that parallel faces of the RVE exhibit the same deformation/orientations compatibility and enables stress continuity. The details of the period boundary conditions are presented in the Appendix.

2.1.2. Material model

It has been shown that the brain tissue under quasi-static loading conditions behaves as an incompressible hyperelastic material [5, 39, 77]. From the literature, the Ogden material model is reported as one of the best mechanical models of the white and gray matters [2, 39]. Therefore, the following Ogden material formulation is used for axonal fibers and ECM:

$$U = \sum_{i=1}^{N} \frac{2\mu_i}{\alpha_i^2}\left(\lambda_1^{\alpha_i} + \lambda_2^{\alpha_i} + \lambda_3^{\alpha_i} - 3\right) \tag{3}$$

Where U is the strain energy per unit of reference volume, μ is the shear modulus, α is a material constant that represents nonlinearity of the material, and λ_i indicate the principal stretches. Because the response of axonal fibers and ECM is modeled by an incompressible material, the volumetric term of the potential energy is omitted, which simplifies the material model into two independent constants: μ and α. For both axonal fibers and matrix, an Ogden material model is used. Moreover, hyperelastic material models of neo-Hookean and Moony-Rivlin will also be examined for comparison. The following equations represent the strain energy function of the neo-Hookean and Mooney-Rivlin material models, respectively.

For neo-Hookean:

$$U = C_{10}(\bar{I}_1 - 3) \tag{4}$$

where C_{10} and D_1 are material parameters; $\bar{I}_1$ is the first deviatoric strain invariant.

For Mooney-Rivlin:

$$U = C_{10}(\bar{I}_1 - 3) + C_{01}(\bar{I}_2 - 3) \tag{5}$$

Where C_{10}, C_{01}, and D_1 are material parameters; $\bar{I}_1$ and $\bar{I}_2$ are the first and second deviatoric strain invariant, respectively.

2.1.3. Embedded element method

A well-established method of modeling a composite material by embedded fibers in a matrix is employed [78–82]. In this technique, the translation degrees of freedom (DOF) of embedded nodes are constrained to the interpolated values of the corresponding DOFs of the host element. Using the embedded element method to create a heterogeneous RVE has distinct advantages. First, the mesh is structurally regular,

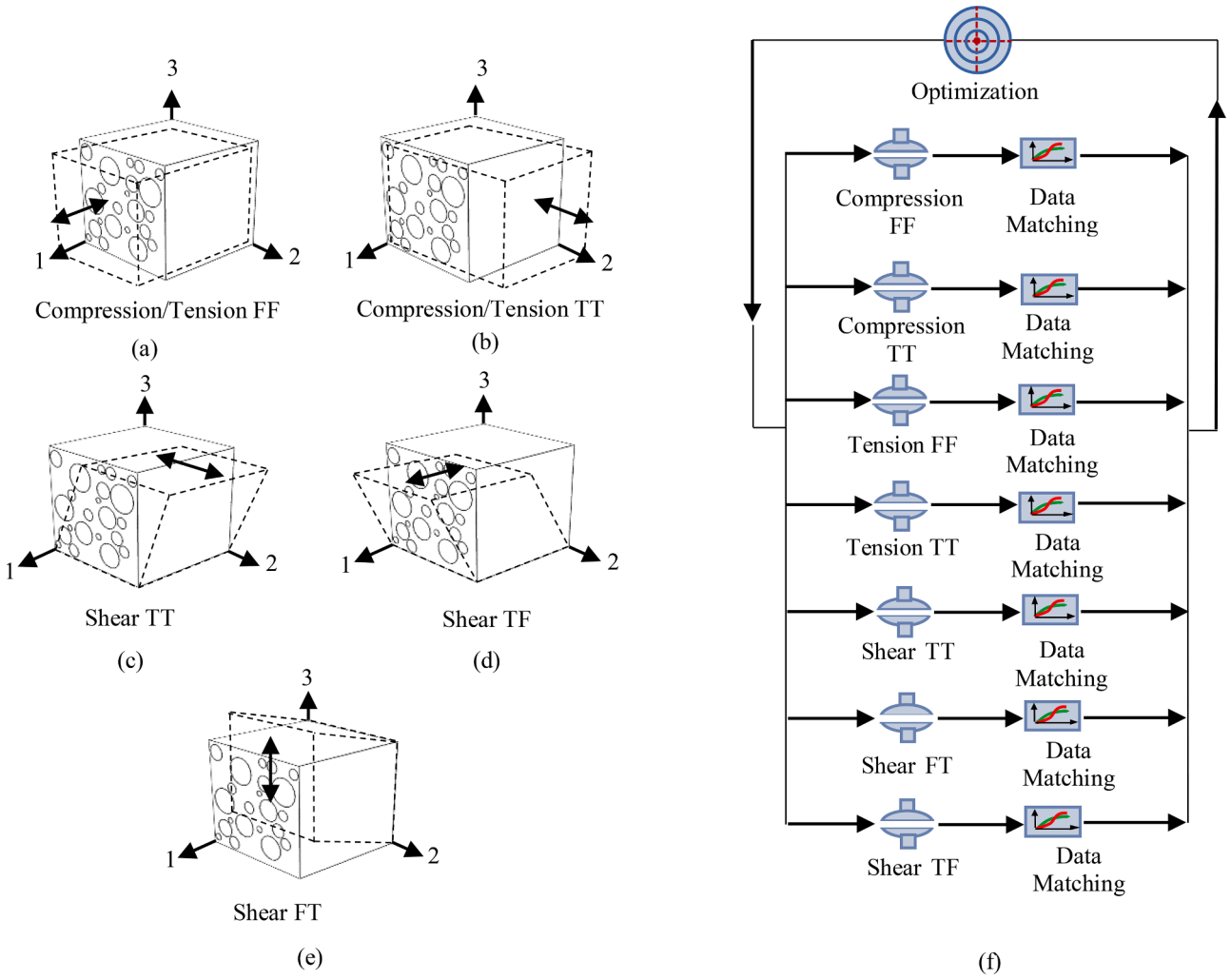

Fig. 4. Seven loading modes for the experimental tests and optimization flowchart. a) Compression/tension along axonal fibers direction. b) Compression/tension in transverse to the axonal fiber direction. c) Shear on the transversal face along the transversal direction of axonal fibers. d) Shear on transversal face along the axonal fibers' direction. e) Shear on fibers face along the transversal direction of axonal fibers. f) Optimization cycle flowchart.

which makes finding the pair of nodes easier. The independent meshing of constituent parts also reduces the total number of elements, which reduces computational costs. The model is created with two domains: a guest domain or fibers and a host domain or matrix. The guest domain itself contains two material properties: the material property of the fiber and the material property of the matrix. Because fibers are embedded in the matrix, the material property of the matrix is added to the material property of the fiber. Thus, there are two material models in a single domain. From superposition, the total strain energy density of this domain can be written as follows:

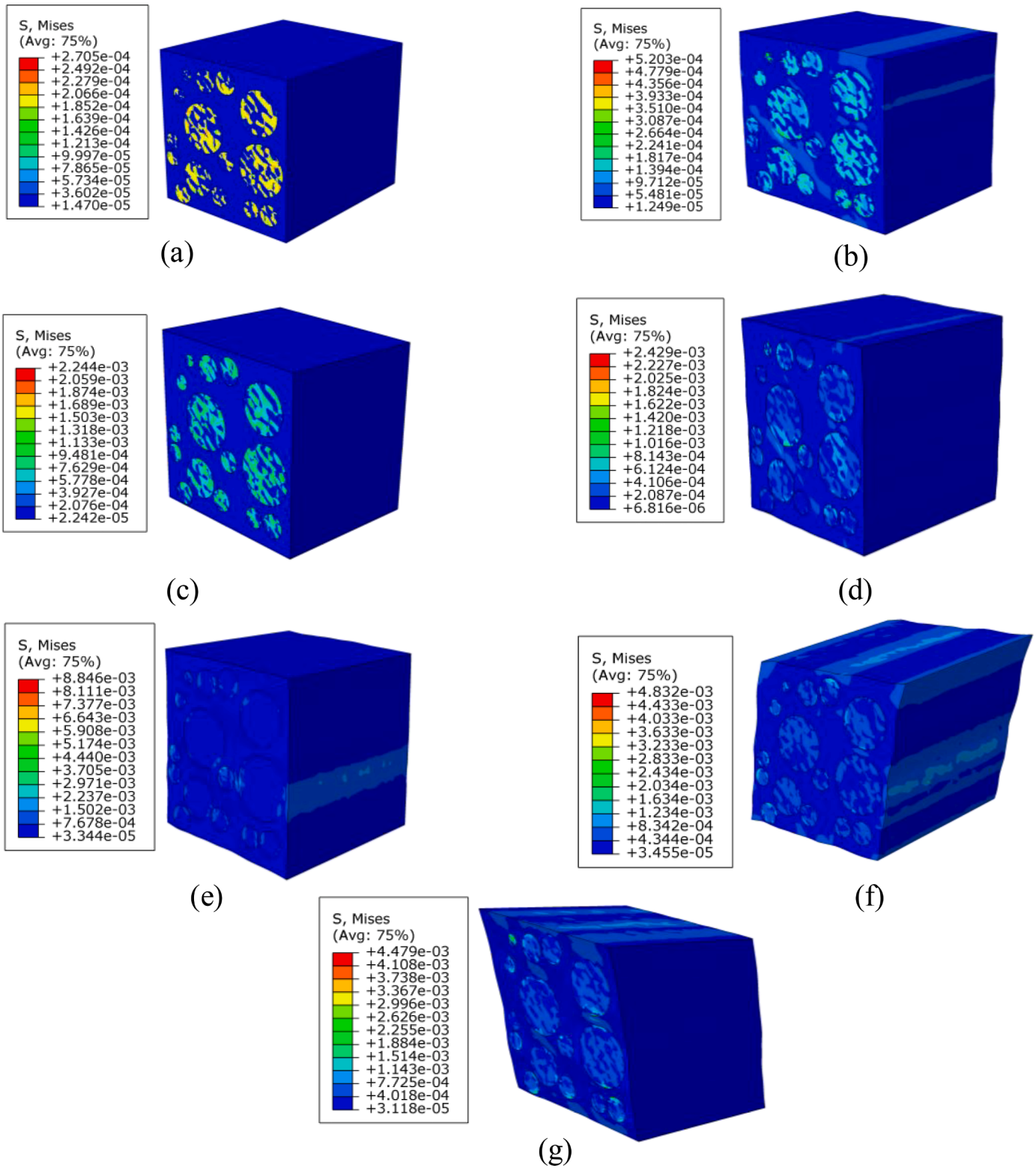

Fig. 5. Deformed von Mises stress contour of a sample RVE under different loading modes. a) Tension-FF, b) Tension-TT, c) Compression-FF, d) Compression-TT, e) Shear-FT, f) Shear-TT, and (g) Shear TF. Applied normal and shear stains in the models is 20%. Fiber volume fraction (FVF) of the model is 0.4. FF denotes aligned with the axonal fibers, while TT denotes transverse to the axonal fibers.

$$W_t(\lambda_1,\lambda_2,\lambda_3) = W_g(\lambda'_1,\lambda'_2,\lambda'_3) + W_h(\lambda''_1,\lambda''_2,\lambda''_3) \quad (6)$$

where $\lambda_{i=1,2,3}$ are terms of principal stretches and W_g and W_h are the strain energy density of the guest and host domains, respectively. The substitution of the Ogden material model in Eq. 6 results in

$$W_t(\lambda_1,\lambda_2,\lambda_3) = \frac{2\mu_g}{\alpha_g^2}\left(\lambda_1^{'\alpha_g},\lambda_2^{'\alpha_g},\lambda_3^{'\alpha_g}-3\right) + \frac{2\mu_h}{\alpha_h^2}\left(\lambda_1^{''\alpha_h},\lambda_2^{''\alpha_h},\lambda_3^{''\alpha_h}-3\right) \quad (7)$$

where μ_g, α_g, μ_h, and α_h are material constants of guest and host domains, respectively. To simplify the material model, almost all prior studies that use this methodology consider an identical value of α for both guest and host domains. While Eq. 7 is simplified with this assumption to a one-term Ogden material model with $\mu = \mu_g + \mu_h$, the significant difference between the composition of axonal fibers and ECM from the biological point of view makes the assumption unrealistic [18, 19, 66, 67]. Instead, we alternatively consider two different material models for axonal fibers and ECM with independent material constants. Considering the point that in the embedded element method the DOFs of corresponding nodes of the guest and host domains are fully coupled, the principal stretches are equal. Therefore, Eq. 7 reduces to

$$W_t(\lambda_1,\lambda_2,\lambda_3) = \frac{2\mu_g}{\alpha_g^2}\left(\lambda_1^{\alpha_g}+\lambda_2^{\alpha_g}+\lambda_3^{\alpha_g}-3\right) + \frac{2\mu_h}{\alpha_h^2}\left(\lambda_1^{\alpha_h}+\lambda_2^{\alpha_h}+\lambda_3^{\alpha_h}-3\right) \quad (8)$$

Eq. 8 can be considered as a two-term Ogden material model. Consequently, the material property of the axonal fiber can be expressed by a two-term Ogden material model with constants derived from the host (matrix) and the guest (embedded fiber). In another words, if the model is created based on the embedded element method, the material property of the embedded axonal fiber is a one-term Ogden material model with μ_g, α_g constants. However, if the model created with separate matrix and fibers (direct mesh method), the material property of the axonal fiber is a two-term Ogden material model with μ_g, α_g, μ_h, and α_h constants. In this study, μ_{f_E} and α_{f_E} represent the material property of the axonal fiber in the embedded format, and μ_f and α_f represent the actual material properties of the axonal fiber.

Optimization process

An optimization process is developed to enable the material properties of axonal fibers and ECM to be inversely calculated from the experimental mechanical data of bulk CC. Fig. 4(a)-(e) shows a schematic of the seven different experimental loading modes that prior studies have performed on human bulk CC [2]. These are compression and tension modes both aligned and orthogonal to the axonal fiber orientation, and three simple shear modes. Fig. 4(f) shows a flowchart of the optimization process. An archive-based microgenetic algorithm is used to implement the multiobjective optimization cycle. The optimization process finds four independent variables: μ_{f_E}, α_{f_E}, μ_{ECM}, and α_{ECM}. For each set of variables, seven simulations are performed, which correspond to the seven loading modes. For each cycle, the sum of the absolute area difference between the stress-strain curve of the simulation and the experiment is calculated. The objective of the optimization cycle is to collectively minimize sum of the absolute area difference between the stress-strain curve of the experiment and simulation for all seven loading modes. The algorithm population size was n=40 and 1500 iterations were performed in total. Further, to minimize simulation costs, all variables were defined as discrete values in a specific limited boundary, consistent with prior literature [62, 80]. The boundary for the variables is set to $\mu_{fE} \in$ [100 2000] *Pa* with step size of 2*Pa*, $(\alpha_{ECM}, \alpha_{fE}) \in$ [−3030] with step size of 1 except [-1, 0, 1], and $\mu_{ECM} \in$ [1500] *Pa* with step size of 2*Pa*. The insensitivity of the optimization process to the randomly selected initial values was checked by running the process for five different initial values.

3. Results and discussions

An RVE is developed to enabled inverse independent characterization of axonal fiber and ECM mechanical properties from the bulk mechanical properties of human CC tissue. Fig. 5 shows the von Mises stress contour for the developed RVE under seven different loading modes. The RVE in Fig. 5 corresponds to the smallest dimensions of brain white matter with mechanical properties identical to those of the bulk tissue. As the embedded element method is used in the RVE, two materials overlap in the axonal fiber sections. Therefore, the cross-sections of axonal fibers are blurry. Fig. 5 (a) and (c) show contours of tension and compression along the axonal fiber direction, respectively. In these cases, the effect of the periodic boundary condition is negligible. However, this effect is more profound in the three shear modes, and compression and tension transverse to the axonal fiber direction, Fig. 5 (b), (d), (e), and (f).

Fig. 6 shows the results of the size and mesh convergence studies for the developed RVE. The nominal stresses in the RVE are calculated by dividing the total reaction force by the initial surface area. Here, the calculated nominal stresses are normalized with respect to μ_{ECM} to enable comparisons to be made between the different loading modes.

Fig. 6(a) indicates that for the cases with edge size of 5, 6 and 7, μm all the loading modes produce the same results. As such, an edge length of 5 μm was chosen as the RVE size. Fig. 6(b) shows the result of the mesh convergence study. Changes in the nominal normalized stress are plotted against the number of mesh nodes in the range ~25,000 to 75,000. The stress becomes independent of the mesh approaching 55,000 nodes. This number was therefore chosen to be the mesh size.

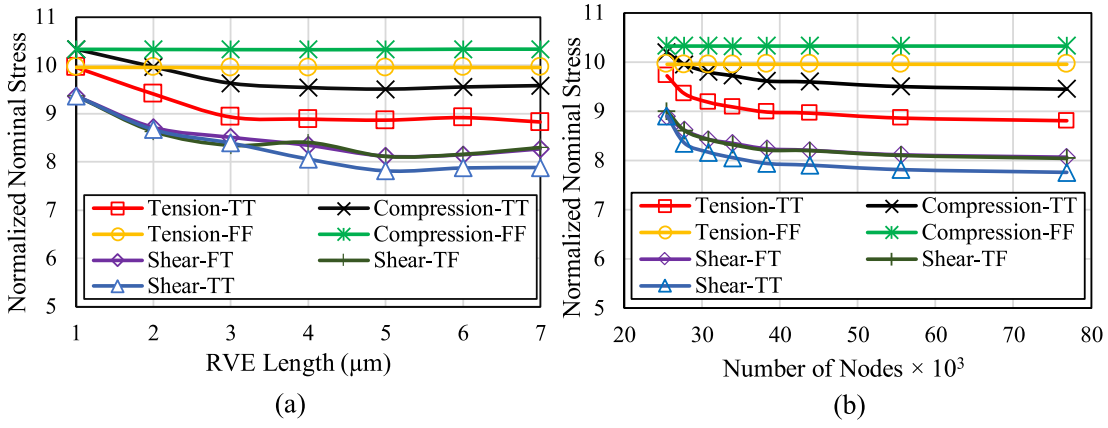

Fig. 6. Size and mesh convergence studies of the developed RVE. a) Normalized nominal stress versus size of RVE for the different loading modes. b) Normalized nominal stress versus mesh size of the RVE with 5μm edge length.

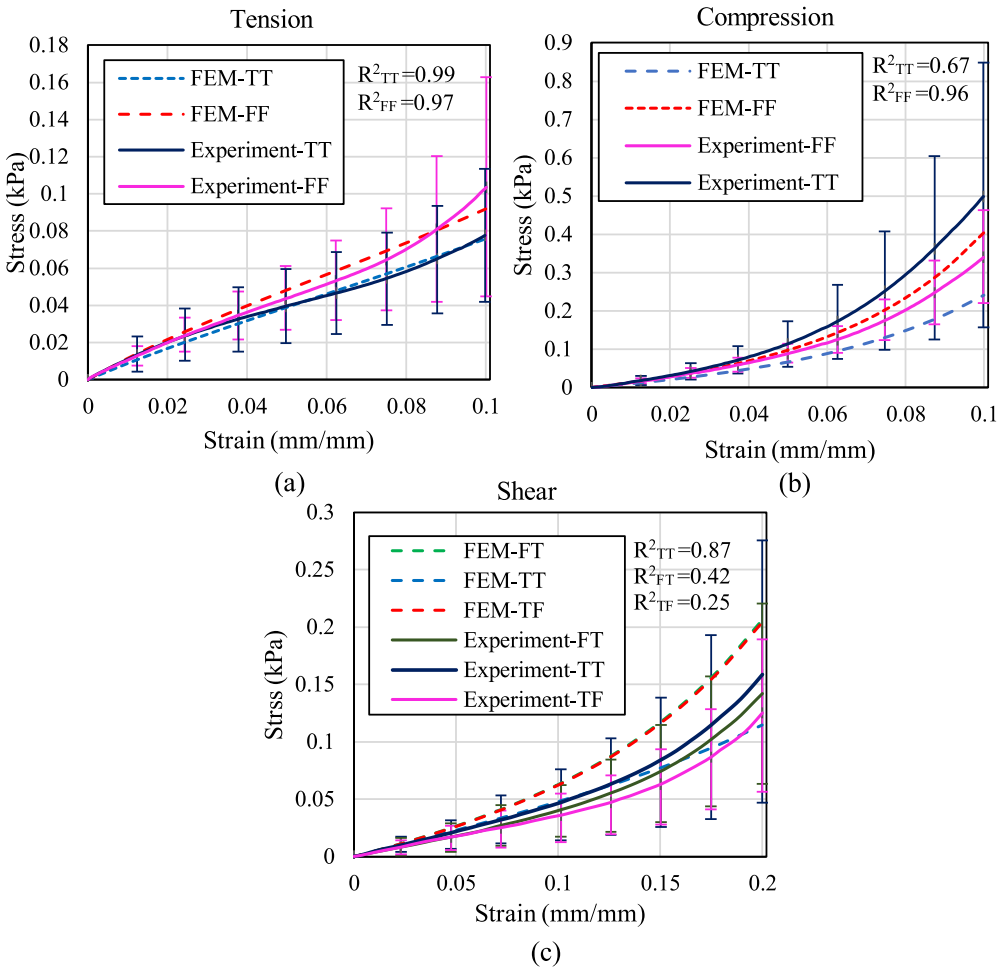

Fig. 7. The mechanical response of the RVE according to the optimized material properties by seven loading modes in comparison with the experimental data in Ref. [2]. Mechanical behavior under a) tension; b) Compression; c) Shear. Error bars show the standard deviations of the experimental tests. FF denotes the alignment with the axonal fibers, while TT denotes transverse to the axonal fibers. FT denotes shear within a plane both aligned and transverse to the axonal fibers.

Budday et al. report that a one-term modified Ogden hyperelastic constitutive model can accurately predict the bulk material properties of CC mechanical behavior under different loadings (tension, compression, shear). Seven stress-strain experimental curves from Ref. [2] associated with the seven loading modes in Fig. 4(a)-(e) of the bulk CC are used as the constitutive model of the RVE hyperelasticity. Then, the seven loading modes simultaneous optimization process inversely predicts the hyperelastic material coefficients of axonal fibers and ECM from the hyperelastic mechanical properties of the bulk CC.

Using this model, the optimization process predicts the following: $\mu_{f_E} = 756 \pm 2$ Pa, $\alpha_{f_E} = -24 \pm 1$, $\mu_{ECM} = 106 \pm 2$ Pa, and $\alpha_{ECM} = -14 \pm 1$. These values minimize the sum of the absolute area difference in stress-strain curve between experiments and simulations for the seven loading modes. Negative values for both α_{f_E} and α_{ECM} capture the asymmetric behavior of the brain tissue in the compression-tension tests. Fig. 7 compares the experimental stress-strain curves for the bulk CC tissue with the generated stress-strain curves by the optimized values.

The RVE's stress-strain curves are based on best fitting the model to the seven different experimental stress-strain curves simultaneously. Fig. 7 shows that the optimized model and associated constitutive axonal fiber and ECM material coefficients accurately predicts the mechanical response of bulk CC tissue for numerous loading conditions, in particular under tension both aligned and orthogonal to the axonal fibers. However, discrepancies exist between simulated and experimental results for compressive loading orthogonal to the axonal fibers, shear FT, and shear TF. Nonetheless, predicted macroscale loading responses fall within the uncertainty of the experimental data, with the exception of the shear TF loading mode. During the optimization process, compression orthogonal to the axonal fiber orientation considerably affects the accuracy of the other loading modes. Experimental results indicate that the CC is stiffer when compressed orthogonally to the axonal fibers relative to compression aligned with the fibers [2]. However, the developed model shows an opposite behavior. While the stiff axonal fibers would be more engaged in the aligned configuration, compressive loading orthogonal to the axonal fiber direction would be expected to be governed predominantly by the mechanical properties of the compliant ECM. As speculation, however, the composite shows a softer response along fibers' direction when axonal fibers show a tension-compression asymmetry behavior or buckling happens in axonal fibers. In our work, because we have assumed a very wide nonlinearity range for axonal fibers and ECM, the material nonlinearity, e.g., tension-compression asymmetry, is not the reason for the poor fitting in one of the seven loading modes. In the RVE, because the length-to-diameter ratio of fibers is not realistic and possesses a small value, fibers cannot buckle inside the matrix. As a result, the modeled composite shows a greater stiffness in the compression along the fibers compared to the transversal compression. Furthermore, because the experimental results are averaged for all the samples, those curves are not for a single sample; therefore, it is expected that a simultaneous optimization for seven loading modes will not perfectly fit to all experimental curves. We speculate that another source of the discrepancy is due to the sizable standard deviations of the compression test

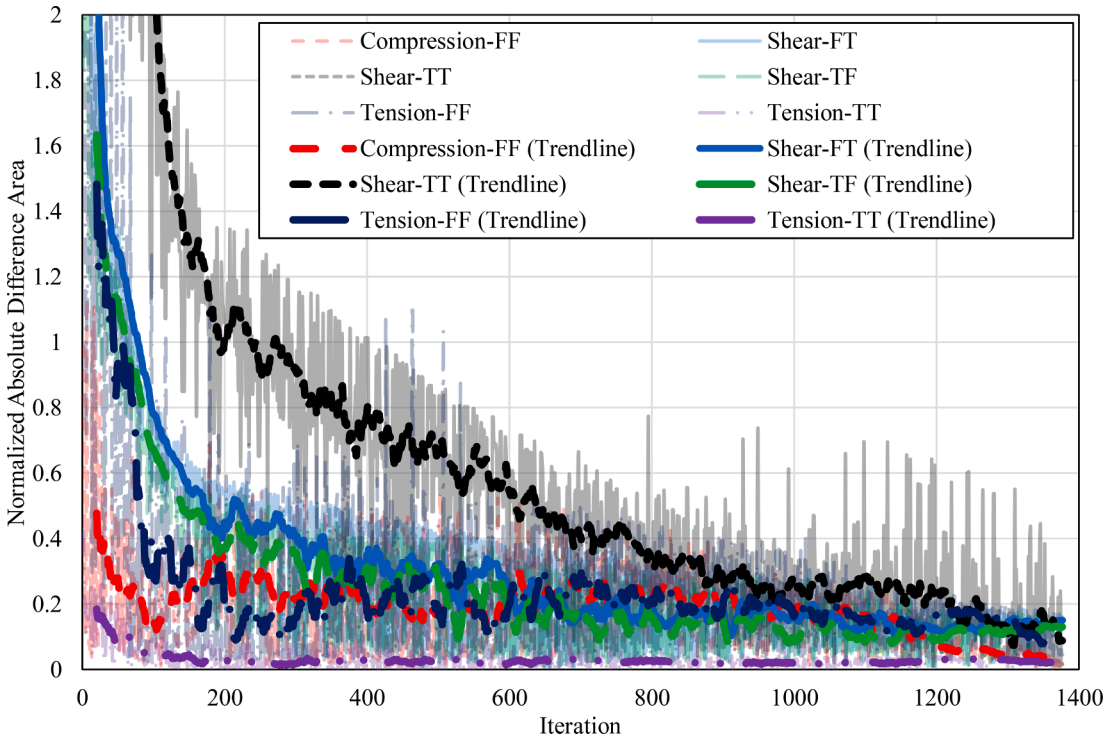

Fig. 8. Normalized absolute area difference between the stress-strain curves of the six loading modes of the experimental data and the modeled RVE during the simultaneous optimization.

transverse to the axonal fibers. There are still samples in Fig. 7(b) that show stiffer response in compression along the fibers than the orthogonal compression. The optimization process has been applied to the RVE with a unique architecture in all loading modes, while the experimental data have been collected and averaged from several samples, which means their mean response is not representative for all individual samples. It also should be mentioned that the model is based on a structure with a specific FVF, while experimental results are established from several tests with samples that have intrinsically varying FVF values.

To establish if the optimization of this specific compressive loading mode limited the overall accuracy of predictions for the other six loading modes, the model was reoptimized excluding the compression mode orthogonal to the axonal fiber direction. Fig. 8 demonstrates the variation of the absolute value of the normalized area difference between the stress-strain curves of the experimental data and RVE results for each loading mode in each iteration for the optimization with the six loading modes. The transparent lines show the normalized area difference in each iteration, and the solid curves show the 20-period moving average trendline of each loading mode during the optimization process. To make the results comparable, for each loading mode, the absolute area difference is normalized by scaling by the corresponding surface area under the experimental stress-strain curve. The aborted analyses, repeated results, and the early outlier data have not been presented in Fig. 8. The trendlines indicate that in all loading modes, the normalized absolute area difference decreases during optimization.

Results of the optimized model, shown in Fig. 9, show a better fit to the experimental results. In comparison with the model optimized to seven loading modes, the results of this new model do not exhibit discrepancies of shear FT or shear TF. Simulated FF compression loading mechanical results are also improved. The reoptimized model predicts the following: $\mu_{f_E} = 722 \pm 2$ Pa, $\alpha_{f_E} = -23 \pm 1$, $\mu_{ECM} = 110 \pm 2$ Pa, and $\alpha_{ECM} = -6 \pm 1$. Fig. 9 further compares the optimum response of the models with the experimental data and model predictions by Hoursan et al. [80] for tensile loading aligned and orthogonal to the axonal fiber directions. The results show a notably improved fit compared to the previous model for compression and shear loading modes. However, predictions for compression orthogonal to fiber alignment remain poor. Results of the previous model shown in Fig. 9 are in places established from the material coefficients presented in their work, given that they did not directly report predictions for the compressive loading modes. This model considered a 30% FVF. As such, an RVE with 30% FVF was created and used to obtain the predictions shown. We anticipate that the optimized material parameter predictions reported here provide more accurate mechanical properties of fiber and ECM mechanical properties, which will aid in improving the accuracy of future computational models that examine multiaxial loading of brain tissues.

In many prior studies of bulk white and gray matter mechanical behavior, neo-Hookean and Moony-Rivlin constitutive models have been utilized [45, 83–87]. These material models are easy to implement in finite element models. To ensure a comprehensive assessment of this predictive model, optimization processes for the six loading modes (excluding compression TT) were completed to obtain the optimal ECM and axonal fiber material coefficients using neo-Hookean and Moony-Rivlin constitutive models. From Eq. 7, the shear modulus of axonal fibers can be simply established by summing the two constituent values, $\mu_f = \mu_{f_E} + \mu_{ECM}$. The optimization process predicts $\mu_f = 310 \pm 2$ Pa and $\mu_{ECM} = 70 \pm 2$ Pa. Fig. S1 in Supplemental Materials compares the neo-Hookean model predictions with the experimental results. This model adequately predicts the tension and shear behavior of axonal fibers and ECM but fails to capture the responses in both compression loading modes.

Our optimization process for the Moony-Rivlin model predicts the following: $C10_{f_E} = 190 \pm 2$ Pa, $C01_{f_E} = 100 \pm 2$ Pa, $C10_{ECM} = 60 \pm 2$ Pa, and $C01_{ECM} = 6 \pm 2$ Pa. For small strains, the embedded shear modulus of axonal fibers and actual shear modulus of ECM are estimated to be $\mu_{f_E} = 580\ Pa$ and $\mu_{ECM} = 132\ Pa$, respectively. In this material model, the actual material properties of the axonal fibers can be calculated by summation of the embedded axonal fiber and ECM material constants. Thus, the actual material properties of the axon can be rep-

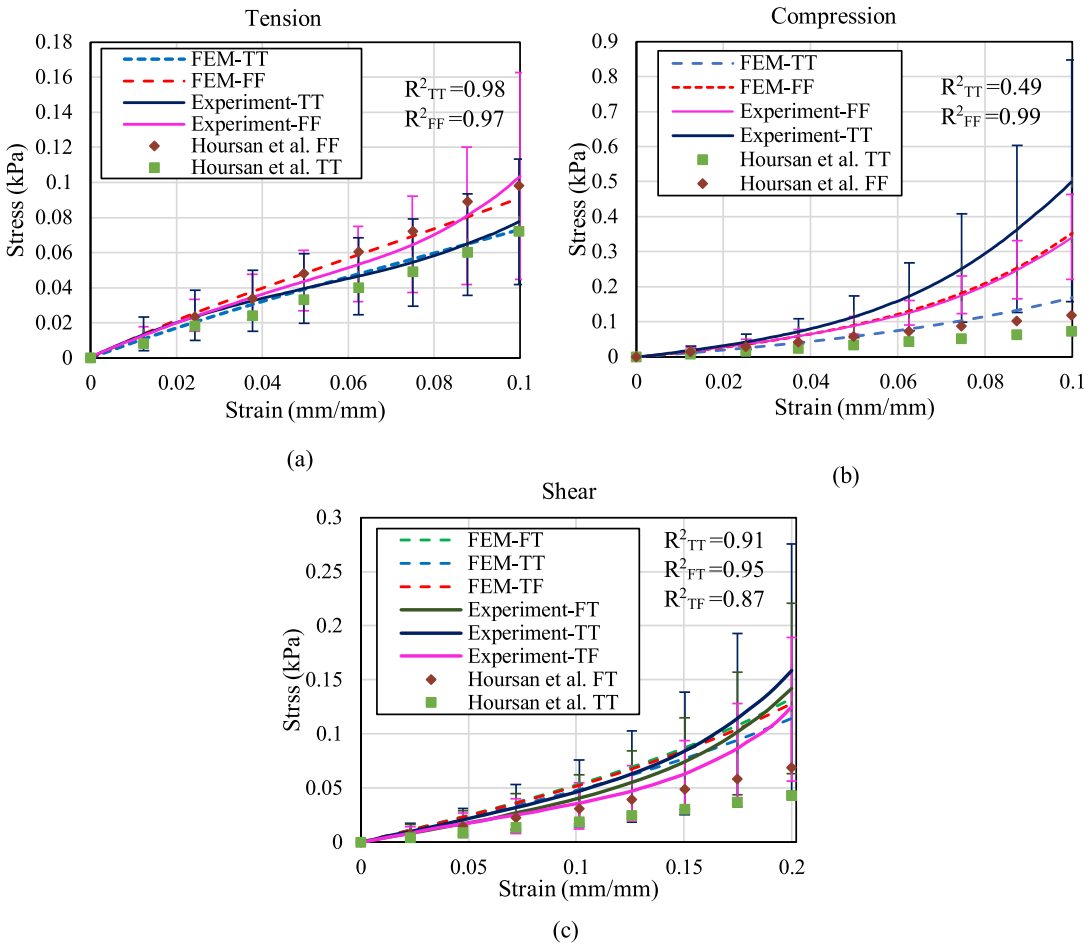

Fig. 9. The mechanical response of the RVE according to the optimized material properties by six loading modes in comparison with the experimental data in [2] and numerical study in [80]. Mechanical behavior under a) Tension; b) Compression; c) Shear. Error bars show the standard deviations of the experimental tests.

Table 2
Comparison of the optimum material constants obtained in present study with values presented in previous studies.

		μ_{axon} (Pa)	α_{axon}	μ_{ECM} (Pa)	α_{ECM}	Reference
Present Study	Embedded Method	722	-23	110	-6	-
	Direct Meshing	μ_1 = 722 μ_2 = 110	α_1 = -23 α_2 = -6	110	-6	-
Hoursan (RVE)		1062.78	4.89	80.12	4.89	[80]
Hoursan (SVE)		738.3	4.49	99.36	4.49	[80]
Yousefsani		1130.3	4.91	87.4	4.91	[81]
Meaney		290.82	6.16	-	-	[65]
Pan		33280	8.22	11093	8.22	[60]

resented by $C10_f = 250\ Pa$ and $C01_f = 106\ Pa$. Fig. S2 shows and compares predicted stress-strain curves with experimental results for the six loading modes. The results indicate that the accuracy of the Moony-Rivlin model is comparable to the neo-Hookean results in Fig. S2. In summary, only an Ogden model is accurate enough to present hyperelastic material behavior of axonal fibers and ECM.

Table 2 shows a comparison between predicted constitutive model coefficients and those from prior studies. While previous micromechanical models can predict the realistic mechanical behavior of CC in a multiaxial loading, they are unable to predict tension-compression asymmetry because they examine only one or two loading modes of the bulk tissue to calibrate their model. From Table 2 there is a wide range of the material constants for both axonal fiber and ECM in the literature. Moreover, prior studies additionally assume the same nonlinearity coefficient, α, for both axonal fibers and ECM, even though axonal fibers and ECM are different materials with different compositions [18, 88]. Hoursan et al. [80] argue that this assumption is made because the nonlinearity will not be sensitive to the loading direction. However, our

Table 3
Summary of the predicted actual material coefficients for axonal fibers and ECM.

Material Model	Material Parameters	Material Parameters Values		R^2						
		Axonal Fiber	ECM	Tension		Compression		Shear		
				FF	TT	FF	TT	FT	TT	TF
Ogden	μ, α	μ_1=722 Pa,α_1= -23,μ_2=110 Pa,α_2= -6	μ=110 Pa, α=-6	0.974	0.989	0.493	0.974	0.954	0.910	0.876
neo-Hookean	μ, α	μ= 380 Pa, α=2	μ=70 Pa, α=2	0.976	0.974	0.459	0.246	0.899	0.829	0.888
Moony-Rivlin	C01, C10	$C10_1$=250, $C01_1$=106 Pa	C10=60,C01=6 Pa	0.975	0.967	0.517	0.254	0.890	0.791	0.900

study shows that there is a considerable difference between the nonlinearity coefficient of axonal fibers and ECM, with α_{f_E} almost twice that of α_{ECM}. Predictions of shear moduli, however, closely align a previous model [80] that has utilized a statistical volume element (SVE) approach. However, nonlinearity coefficients differ between the two studies. Table 2 further reveals that in comparison with the results of the current study, Meaney et al. [65] underestimates the shear modulus of both the axonal fibers, while Hoursan et al. (RVE method) [80], Yousefsani et al. [61], and Pan et al. [60] overestimate it. Our results show that for to capture the tension-compression asymmetry in a single material model, a negative value of the α should be employed. In Table 1, there are two possible representations for the material parameters of axonal fibers. For the studies that use the embedded element method, values in the first row without any material correction can be used for axonal fibers, while the real material properties of axonal fibers for direct meshing models are characterized by a two-term Ogden material model in the second row (see Methods Section).

The results of the optimization process for the three different material models, Ogden, neo-Hookean, and Moony-Rivlin, are summarized in Table 2. Material coefficients in Table 3 can be directly used in finite element packages for the material properties of axonal fibers and ECM.

Fig. S3 shows the stress-strain curves of the axonal fibers and ECM according to the reported values in Table 3. It is clear that the axonal fiber has a greater asymmetry and nonlinearity degree than the ECM. For the ECM, Ogden, neo-Hookean, or Mooney-Rivlin hyperelastic material models can each be used with a reasonable accuracy. However, only an Ogden model is sufficiently accurate for axonal fibers.

The measurement of the mechanical properties of the axonal fibers when coupled with imaging data (DTI, fiber tractography) may offer new tools to overcome the disadvantages of MRE and identify or evaluate brain disorders such as Alzheimer's, multiple sclerosis, and autism. Findings of this study have a direct and important impact on the precise and unbiased computational modeling of TBI/DAI and brain folding that include axonal fiber bundles [46, 89, 90]. In TBI/DAI computational models, in addition to the hyperelastic material behavior, the viscoelastic material behavior of axonal fibers and ECM should be included. However, the characterization of the viscoelastic behavior of axonal fibers and ECM was not a scope of this study.

Similar to other computational modeling studies, there are a few limitations in this study: a) Only parallel axonal fibers were considered in RVE, while *in vivo* axonal fibers can have a distribution of orientations. However, the effect of this limitation is negligible as the CC has highly aligned axonal fiber bundles; b) Circular cross-sections were used for the axonal fibers, while axonal fibers typically have nonsymmetric or elliptical cross-section profiles (Fig. 1). However, our results (not reported here) showed that the distribution of axonal fibers' diameter has a negligible effect on the simulation results. The diameter distribution has no effect on tension and compression and is negligible in shear; c) The optimized material coefficients predicted are for the combined axon and myelin sheath as a composite material. Those values cannot be used exclusively for the axon or the myelin independently. d) The most important parameter that has a considerable effect on the results is the FVF. All predictions are based on an *FVF* of 40%. By increasing or reducing the FVF, new optimum material coefficients will be achieved. Fig. S4 demonstrates that an increase in the percentage of axonal fibers in the matrix results in a greater stiffness of the tissue. Therefore, the precise determination of FVF in CC by electron microscopy or any other experimental tool could increase the accuracy of the results; e) The brain tissue also shows viscoelastic and poroelastic behaviors [8, 54]. The viscoelasticity was not considered in this study because in a quasi-static loading condition the effect of viscosity is negligible. To find the associated viscoelastic material properties of axonal fibers and ECM, another optimization process with different material parameters is needed. f) The used RVE was simple enough to be able to perform the optimization process including finite element simulations in order of thousands. This simplification can affect the fitting results. Adding more complexity, e.g. buckling, into the RVE might well model the actual tissue composition. An experiment-based customized RVE is required to get more accurate predictions. Finally, g) The predicted constitutive coefficients are established by fitting the hyperelastic model to experimental measurements of excised CC, which themselves contain inherent uncertainties.

4. Conclusion

In this study, the independent hyperelastic mechanical properties of myelinated axonal fibers and the surrounding extracellular matrix (ECM) are extracted from macroscale mechanical measurements of corpus callosum (CC) white matter tissue using a microstructural modeling and an optimization process. Results of the study show that an Ogden incompressible hyperelastic material model can accurately predict the mechanical behavior of axonal fibers and ECM. Both axonal fibers and ECM show a highly nonlinear behavior under different loading modes. However, the degree of the nonlinearity in axonal fibers is greater than the ECM, in opposition to the previous assumptions for considering similar nonlinearity coefficients. In addition to the Ogden model, the material coefficients for neo-Hookean and Moony-Rivlin hyperelastic models were predicted and discussed. Alterations of microscale constituents of the brain tissue greatly impact the mechanical properties of the tissue at the macroscale.

The hyperelastic material properties for axonal fibers and ECM presented in this study are more accurate than previously proposed because they have been optimized using seven or six loading modes of the bulk tissue, not just one or two. Therefore, predicted values can be used to improve and update other modeling studies that relate to traumatic brain injury, deep brain stimulation probe insertion, brain folding, and fluid-solid interactions in the brain.

Data availability

The data that support the findings of this study are available from the corresponding author upon reasonable request.

Credit authorship contribution statement

Poorya Chavoshnejad: Methodology, Formal analysis, Software, Writing – original draft. Guy K German: Validation, Writing – review & editing. Mir Jalil Razavi: Conceptualization, Investigation, Supervision, Writing – review & editing, Funding acquisition.

Declaration of Competing Interest

The authors declare that they have no known competing financial interests or personal relationships that could have appeared to influence the work reported in this paper.

Acknowledgement

This research was partially supported by the National Science Foundation [2123061] and TAE health-science seed grant from Binghamton University. This work used the Extreme Science and Engineering Discovery Environment (XSEDE) for a part of the computational simulations, which is supported by National Science Foundation [ACI-1548562].

Supplementary materials

Supplementary material associated with this article can be found, in the online version, at doi:10.1016/j.brain.2021.100035.

Appendix

Fig. A1 and equations A1-A10 illustrate the relation between mesh nodes on faces, edges, and corner points of the RVE.

$$(u_i)_{c_j} + (u_i)_{c_k} = 0,\ i=1,2,3,\ \{\begin{matrix} j=2 \\ k=1 \end{matrix},\ \begin{cases} j=4 \\ k=3 \end{cases},\ \begin{cases} j=6 \\ k=5 \end{cases} \tag{A1}$$

$$(u_i)_{F_j} + (u_i)_{F_k} + 2(u)_{c_k} = 0,\ i=1,2,3,\ \{\begin{matrix} j=2 \\ k=1 \end{matrix},\ \begin{cases} j=4 \\ k=3 \end{cases},\ \begin{cases} j=6 \\ k=5 \end{cases} \tag{A2}$$

$$(u)_{E_{jk}} + (u)_{E_{lm}} + 2\left((u_i)_{c_l} - (u)_{c_k}\right) = 0, \tag{A3}$$

$$i=1,2,3,\ \{\begin{matrix} jk=23 \\ lm=14 \end{matrix},\ \begin{cases} jk=25 \\ lm=16 \end{cases},\ \begin{cases} jk=46 \\ lm=36 \end{cases}$$

$$(u_i)_{E_{jk}} + (u_i)_{E_{lm}} + 2\left((u_i)_{c_l} + (u_i)_{c_m}\right) = 0, \tag{A4}$$

$$i=1,2,3,\ \{\begin{matrix} jk=24 \\ lm=13 \end{matrix},\ \begin{cases} jk=26 \\ lm=15 \end{cases},\ \begin{cases} jk=46 \\ lm=35 \end{cases}$$

$$(u_i)_{C_{235}} + (u_i)_{C_{146}} + 2\left((u_i)_{c_1} - (u_i)_{c_3} - (u_i)_{c_5}\right) = 0,\ i=1,2,3 \tag{A5}$$

$$(u_i)_{C_{236}} + (u_i)_{C_{145}} + 2\left((u_i)_{c_1} - (u_i)_{c_3} + (u_i)_{c_5}\right) = 0,\ i=1,2,3 \tag{A6}$$

$$(u_i)_{C_{245}} + (u_i)_{C_{136}} + 2\left((u_i)_{c_1} + (u_i)_{c_3} - (u_i)_{c_5}\right) = 0,\ i=1,2,3 \tag{A7}$$

$$(u_i)_{C_{246}} + (u_i)_{C_{135}} + 2\left((u_i)_{c_1} + (u_i)_{c_3} + (u_i)_{c_5}\right) = 0,\ i=1,2,3 \tag{A8}$$

where F_i, E_{ij}, C_{ijk}, and c_i imply faces, edges, corners, and centers of the RVE, respectively. u_i (i=1, 2, 3) shows displacement of each node on a face, edge, corner, or center of the RVE along the 1, 2, and 3 directions, respectively. Using these equations, the displacement of each slave node on faces (F_2, F_4, F_6), edges (E_{23}, E_{24}, E_{25}, E_{26}, E_{45}, E_{46}), centers (c_2, c_4, c_6), and corners (C_{235}, C_{236}, C_{245}, C_{246}) is related to their relevant master nodes on faces (F_1, F_3, F_5), edges (E_{14}, E_{13}, E_{16}, E_{15}, E_{36}, E_{35}), centers (c_1, c_3, c_5), and corners (C_{146}, C_{145}, C_{136}, C_{135}), respectively. Finding pair nodes and applying these constraints are implemented using a Python script in Abaqus.

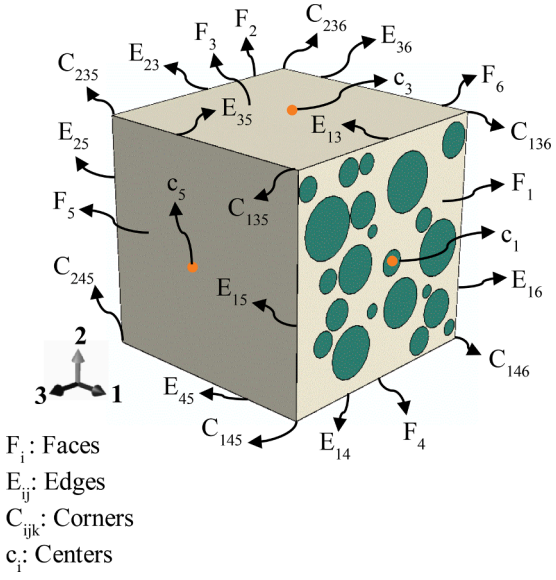

Fig. A1. Definition of the face, centers, edges, and corners of RVE for the application of periodic boundary condition.

References

[1] S Budday, P Steinmann, E. Kuhl, Physical biology of human brain development, Front Cell Neurosci 9 (2015), https://doi.org/10.3389/fncel.2015.00257.

[2] S Budday, G Sommer, C Birkl, C Langkammer, J Haybaeck, J Kohnert, et al., Mechanical characterization of human brain tissue, Acta Biomater. 48 (2017) 319–340.

[3] S Budday, R Nay, R de Rooij, P Steinmann, T Wyrobek, TC Ovaert, et al., Mechanical properties of gray and white matter brain tissue by indentation, J. Mech. Behav. Biomed. Mater. 46 (2015) 318–330.

[4] R Moran, JH Smith, JJ. García, Fitted hyperelastic parameters for Human brain tissue from reported tension, compression, and shear tests, J. Biomech. 47 (2014) 3762–3766.

[5] T Kaster, I Sack, A. Samani, Measurement of the hyperelastic properties of ex vivo brain tissue slices, J. Biomech. 44 (2011) 1158–1163.

[6] S Budday, TC Ovaert, GA Holzapfel, P Steinmann, E. Kuhl, Fifty Shades of Brain: A Review on the Mechanical Testing and Modeling of Brain Tissue, Arch Computat Methods Eng (2019), https://doi.org/10.1007/s11831-019-09352-w.

[7] S Chatelin, A Constantinesco, R Willinger, Fifty years of brain tissue mechanical testing: From in vitro to in vivo investigations, Biorheology 47 (5–6) (2010) 255–276. :.

[8] E Comellas, S Budday, J-P Pelteret, GA Holzapfel, Steinmann P. Modeling the porous and viscous responses of human brain tissue behavior, Comput. Meth. Appl. Mech. Eng. 369 (2020), 113128.

[9] S Budday, G Sommer, GA Holzapfel, P Steinmann, E. Kuhl, Viscoelastic parameter identification of human brain tissue, J. Mech. Behav. Biomed. Mater. 74 (2017) 463–476.

[10] MT Prange, SS. Margulies, Regional, Directional, and Age-Dependent Properties of the Brain Undergoing Large Deformation, J. Biomech. Eng. 124 (2002) 244–252.

[11] X Ning, Q Zhu, Y Lanir, SS. Margulies, A Transversely Isotropic Viscoelastic Constitutive Equation for Brainstem Undergoing Finite Deformation, J. Biomech. Eng. 128 (2006) 925–933.

[12] F Velardi, F Fraternali, M. Angelillo, Anisotropic constitutive equations and experimental tensile behavior of brain tissue, Biomech. Model. Mechanobiol. 5 (2006) 53–61.

[13] Y Feng, RJ Okamoto, R Namani, GM Genin, PV. Bayly, Measurements of mechanical anisotropy in brain tissue and implications for transversely isotropic material models of white matter, J. Mech. Behav. Biomed. Mater. 23 (2013) 117–132.

[14] N Liu, P Chavoshnejad, S Li, MJ Razavi, T Liu, R Pidaparti, et al., Geometrical nonlinear elasticity of axon under tension: A coarse-grained computational study, Biophys. J. 120 (2021) 3697–3708.

[15] SJ Peter, MRK. Mofrad, Computational Modeling of Axonal Microtubule Bundles under Tension, Biophys. J. 102 (2012) 749–757.

[16] PW Baas, AN Rao, AJ Matamoros, L. Leo, Stability properties of neuronal microtubules, Cytoskeleton (Hoboken) 73 (2016) 442–460.

[17] Y Poitelon, AM Kopec, S. Belin, Myelin Fat Facts: An Overview of Lipids and Fatty Acid Metabolism, Cells 9 (2020) 812.

[18] Brady ST, Siegel GJ, Albers RW, Price DL. Basic neurochemistry: principles of molecular, cellular, and medical neurobiology. 2012.

[19] J Weickenmeier, R de Rooij, S Budday, TC Ovaert, E. Kuhl, The mechanical importance of myelination in the central nervous system, J. Mech. Behav. Biomed. Mater. 76 (2017) 119–124.

[20] J Weickenmeier, R de Rooij, S Budday, P Steinmann, TC Ovaert, Kuhl E. Brain stiffness increases with myelin content, Acta Biomater. 42 (2016) 265–272.

[21] F Aboitiz, AB Scheibel, RS Fisher, Zaidel E. Fiber composition of the human corpus callosum, Brain Res. 598 (1992) 143–153.

[22] N Stikov, LM Perry, A Mezer, E Rykhlevskaia, BA Wandell, JM Pauly, et al., Bound pool fractions complement diffusion measures to describe white matter micro and macrostructure, Neuroimage 54 (2011) 1112–1121.

[23] R Caminiti, F Carducci, C Piervincenzi, A Battaglia-Mayer, G Confalone, F Visco-Comandini, et al., Diameter, Length, Speed, and Conduction Delay of Callosal Axons in Macaque Monkeys and Humans: Comparing Data from Histology and Magnetic Resonance Imaging Diffusion Tractography, J. Neurosci. 33 (2013) 14501–14511.

[24] I Cinelli, M Destrade, P McHugh, M. Duffy, Effects of nerve bundle geometry on neurotrauma evaluation, Int. J. Numer. Meth. Biomed. Engng. 34 (2018) e3118.

[25] D Liewald, R Miller, N Logothetis, H-J Wagner, A. Schüz, Distribution of axon diameters in cortical white matter: an electron-microscopic study on three human brains and a macaque, Biol. Cybern. 108 (2014) 541–557.

[26] CL Johnson, MDJ McGarry, AA Gharibans, JB Weaver, KD Paulsen, H Wang, et al., Local mechanical properties of white matter structures in the human brain, Neuroimage 79 (2013) 145–152.

[27] GB Potter, M Santos, MT Davisson, DH Rowitch, DL Marks, ER Bongarzone, et al., Missense mutation in mouse GALC mimics human gene defect and offers new insights into Krabbe disease, Hum. Mol. Genet. 22 (2013) 3397–3414.

[28] KB Arbogast, DF. Meaney, Biomechanical characterization of the constitutive relationship of the brainstem, Proc. Soc. Automotive Eng. (1995) 153–159. :.

[29] A Perry, CS Graffeo, N Fattahi, MM ElSheikh, N Cray, A Arani, et al., Clinical Correlation of Abnormal Findings on Magnetic Resonance Elastography in Idiopathic Normal Pressure Hydrocephalus, World Neurosurg. 99 (2017) 695–700, e1.

[30] FB Freimann, K-J Streitberger, D Klatt, K Lin, J McLaughlin, J Braun, et al., Alteration of brain viscoelasticity after shunt treatment in normal pressure hydrocephalus, Neuroradiology 54 (2012) 189–196.

[31] K-J Streitberger, E Wiener, J Hoffmann, FB Freimann, D Klatt, J Braun, et al., In vivo viscoelastic properties of the brain in normal pressure hydrocephalus, NMR Biomed. (2010). :n/a-n/a.

[32] AA Badachhape, RJ Okamoto, RS Durham, BD Efron, SJ Nadell, CL Johnson, et al., The Relationship of Three-Dimensional Human Skull Motion to Brain Tissue Deformation in Magnetic Resonance Elastography Studies, J. Biomech. Eng. 139 (2017), 051002.

[33] LV Hiscox, CL Johnson, E Barnhill, MDJ McGarry, J Huston, EJR van Beek, et al., Magnetic resonance elastography (MRE) of the human brain: technique, findings and clinical applications, Phys. Med. Biol. 61 (2016) R401–R437.

[34] CL Johnson, EH. Telzer, Magnetic resonance elastography for examining developmental changes in the mechanical properties of the brain, Developmental Cognitive Neuroscience 33 (2018) 176–181.

[35] A Zorgani, R Souchon, A-H Dinh, J-Y Chapelon, J-M Ménager, S Lounis, et al., Brain palpation from physiological vibrations using MRI, Proc Natl Acad Sci USA. 112 (2015) 12917–12921.

[36] MJ Razavi, T Zhang, X Li, T Liu, X. Wang, Role of mechanical factors in cortical folding development, Phys. Rev. E 92 (2015), https://doi.org/10.1103/PhysRevE.92.032701.

[37] T Tallinen, JY Chung, F Rousseau, N Girard, J Lefèvre, L Mahadevan, On the growth and form of cortical convolutions, Nature Phys 12 (2016) 588–593.

[38] S Budday, P Steinmann, E. Kuhl, The role of mechanics during brain development, J. Mech. Phys. Solids 72 (2014) 75–92.

[39] LA Mihai, L Chin, PA Janmey, A. Goriely, A comparison of hyperelastic constitutive models applicable to brain and fat tissues, J. R. Soc. Interface 12 (2015), 20150486.

[40] S Chatelin, C Deck, R. Willinger, An anisotropic viscous hyperelastic constitutive law for brain material finite-element modeling, J. Biorheol. 27 (2013) 26–37.

[41] D Sahoo, C Deck, R. Willinger, Development and validation of an advanced anisotropic visco-hyperelastic human brain FE model, J. Mech. Behav. Biomed. Mater. 33 (2014) 24–42.

[42] RJH Cloots, JAW van Dommelen, MGD. Geers, A tissue-level anisotropic criterion for brain injury based on microstructural axonal deformation, J. Mech. Behav. Biomed. Mater. 5 (2012) 41–52.

[43] C Giordano, S. Kleiven, Connecting fractional anisotropy from medical images with mechanical anisotropy of a hyperviscoelastic fibre-reinforced constitutive model for brain tissue, J. R. Soc. Interface 11 (2014), 20130914.

[44] NC Colgan, MD Gilchrist, KM. Curran, Applying DTI white matter orientations to finite element head models to examine diffuse TBI under high rotational accelerations, Prog. Biophys. Mol. Biol. 103 (2010) 304–309.

[45] HT Garimella, RH. Kraft, Modeling the mechanics of axonal fiber tracts using the embedded finite element method: Axonal fiber mechanics using the embedded element method, Int J Numer Meth Biomed Engng 33 (2017) e2823.

[46] M Hajiaghamemar, T Wu, MB Panzer, SS. Margulies, Embedded axonal fiber tracts improve finite element model predictions of traumatic brain injury, Biomech. Model. Mechanobiol. 19 (2020) 1109–1130.

[47] T Wu, A Alshareef, JS Giudice, MB. Panzer, Explicit Modeling of White Matter Axonal Fiber Tracts in a Finite Element Brain Model, Ann. Biomed. Eng. 47 (2019) 1908–1922.

[48] MC Murphy, DT Jones, CR Jack, KJ Glaser, ML Senjem, A Manduca, et al., Regional brain stiffness changes across the Alzheimer's disease spectrum, NeuroImage: Clinical 10 (2016) 283–290.

[49] MC Murphy, J Huston, CR Jack, KJ Glaser, A Manduca, JP Felmlee, et al., Decreased brain stiffness in Alzheimer's disease determined by magnetic resonance elastography, J. Magn. Reson. Imaging 34 (2011) 494–498.

[50] A Lipp, R Trbojevic, F Paul, A Fehlner, S Hirsch, M Scheel, et al., Cerebral magnetic resonance elastography in supranuclear palsy and idiopathic Parkinson's disease, NeuroImage: Clinical 3 (2013) 381–387.

[51] K-J Streitberger, I Sack, D Krefting, C Pfüller, J Braun, F Paul, et al., Brain Viscoelasticity Alteration in Chronic-Progressive Multiple Sclerosis, PLoS One 7 (2012) e29888.

[52] Z Zhou, AG Domel, X Li, G Grant, S Kleiven, DB Camarillo, et al., White matter tract-oriented deformation is dependent on real-time axonal fiber orientation, J. Neurotrauma (2021). :neu.2020.7412.

[53] D Garcia-Gonzalez, NS Race, NL Voets, DR Jenkins, SN Sotiropoulos, G Acosta, et al., Cognition based bTBI mechanistic criteria; a tool for preventive and therapeutic innovations, Sci. Rep. 8 (2018) 10273.

[54] D Garcia-Gonzalez, A. Jerusalem, Energy based mechano-electrophysiological model of CNS damage at the tissue scale, J. Mech. Phys. Solids 125 (2019) 22–37.

[55] R Bernal, PA Pullarkat, F. Melo, Mechanical Properties of Axons, Phys. Rev. Lett. 99 (2007), 018301.

[56] N Abolfathi, A Naik, M Sotudeh Chafi, G Karami, M Ziejewski, A micromechanical procedure for modelling the anisotropic mechanical properties of brain white matter, Comput. Methods Biomech. Biomed. Eng. 12 (2009) 249–262.

[57] S Javid, A Rezaei, G Karami, A micromechanical procedure for viscoelastic characterization of the axons and ECM of the brainstem, J. Mech. Behav. Biomed. Mater. 30 (2014) 290–299.

[58] G Karami, N Grundman, N Abolfathi, A Naik, M. Ziejewski, A micromechanical hyperelastic modeling of brain white matter under large deformation, J. Mech. Behav. Biomed. Mater. 2 (2009) 243–254.

[59] Yi Pan, DI Shreiber, AA. Pelegri, A Transition Model for Finite Element Simulation of Kinematics of Central Nervous System White Matter, IEEE Trans. Biomed. Eng. 58 (2011) 3443–3446.

[60] Y Pan, D Sullivan, DI Shreiber, AA. Pelegri, Finite Element Modeling of CNS White Matter Kinematics: Use of a 3D RVE to Determine Material Properties, Front Bioeng Biotechnol 1 (2013), https://doi.org/10.3389/fbioe.2013.00019.

[61] SA Yousefsani, A Shamloo, F. Farahmand, Micromechanics of brain white matter tissue: A fiber-reinforced hyperelastic model using embedded element technique, J. Mech. Behav. Biomed. Mater. 80 (2018) 194–202.
[62] SA Yousefsani, A Shamloo, F. Farahmand, Nonlinear mechanics of soft composites: hyperelastic characterization of white matter tissue components, Biomech. Model. Mechanobiol. 19 (2020) 1143–1153.
[63] M Kazempour, M Baniassadi, H Shahsavari, Y Remond, M. Baghani, Homogenization of heterogeneous brain tissue under quasi-static loading: a visco-hyperelastic model of a 3D RVE, Biomech. Model. Mechanobiol. 18 (2019) 969–981.
[64] H Shahsavari, H Jokar, M Haghighi-yazdi, M Baghani, Y Remond, D George, et al., Micromechanical Modeling of the Effective Mechanical Behavior of Cerebral Cortex Tissue, Iran J Sci Technol Trans Mech Eng 44 (2020) 273–285.
[65] DF. Meaney, Relationship between structural modeling and hyperelastic material behavior: application to CNS white matter, Biomech. Model. Mechanobiol. 1 (2003) 279–293.
[66] AD Theocharis, SS Skandalis, C Gialeli, NK. Karamanos, Extracellular matrix structure, Adv. Drug. Deliv. Rev. 97 (2016) 4–27.
[67] U. Rauch, Extracellular matrix components associated with remodeling processes in brain, CMLS, Cell Mol Life Sci. (2004) 61, https://doi.org/10.1007/s00018-004-4043-x.
[68] F Ge, X Li, MJ Razavi, H Chen, T Zhang, S Zhang, et al., Denser Growing Fiber Connections Induce 3-hinge Gyral Folding, Cereb. Cortex 28 (2018) 1064–1075.
[69] MJ Razavi, T Liu, X. Wang, Mechanism Exploration of 3-Hinge Gyral Formation and Pattern Recognition, Cerebral Cortex Communications 2 (2021) tgab044.
[70] T Zhang, MJ Razavi, H Chen, Y Li, X Li, L Li, et al., Mechanisms of circumferential gyral convolution in primate brains, J. Comput. Neurosci. 42 (2017) 217–229.
[71] M Mahdavi, M Baniassadi, M Baghani, M Dadmun, M. Tehrani, 3D reconstruction of carbon nanotube networks from neutron scattering experiments, Nanotechnology 26 (2015), 385704.
[72] CT Sun, RS. Vaidya, Prediction of composite properties from a representative volume element, Compos. Sci. Technol. 56 (1996) 171–179.
[73] K Breuer, M. Stommel, RVE modelling of short fiber reinforced thermoplastics with discrete fiber orientation and fiber length distribution, SN Appl Sci 2 (2020) 91.
[74] E Yousefi, A Sheidaei, M Mahdavi, M Baniassadi, M Baghani, G. Faraji, Effect of nanofiller geometry on the energy absorption capability of coiled carbon nanotube composite material, Compos. Sci. Technol. 153 (2017) 222–231.
[75] Abaqus analysis user's manual, Version 6.13., Dassault System Simula Corp, RI, USA, 2013.
[76] V-D Nguyen, E Béchet, C Geuzaine, L. Noels, Imposing periodic boundary condition on arbitrary meshes by polynomial interpolation, Comput. Mater. Sci. 55 (2012) 390–406.
[77] GZ Voyiadjis, A. Samadi-Dooki, Hyperelastic modeling of the human brain tissue: Effects of no-slip boundary condition and compressibility on the uniaxial deformation, J. Mech. Behav. Biomed. Mater. 83 (2018) 63–78.
[78] T Belytschko, J Fish, BE Engelmann, A finite element with embedded localization zones, Comput. Meth. Appl. Mech. Eng. 70 (1988) 59–89.
[79] SA Tabatabaei, SV Lomov, I. Verpoest, Assessment of embedded element technique in meso-FE modelling of fibre reinforced composites, Compos. Struct. 107 (2014) 436–446.
[80] H Hoursan, F Farahmand, MT. Ahmadian, A Three-Dimensional Statistical Volume Element for Histology Informed Micromechanical Modeling of Brain White Matter, Ann. Biomed. Eng. 48 (2020) 1337–1353.
[81] SA Yousefsani, F Farahmand, A Shamloo, A three-dimensional micromechanical model of brain white matter with histology-informed probabilistic distribution of axonal fibers, J. Mech. Behav. Biomed. Mater. 88 (2018) 288–295.
[82] P Chavoshnejad, AH Foroughi, N Dhandapani, GK German, MJ. Razavi, Effect of collagen degradation on the mechanical behavior and wrinkling of skin, Phys. Rev. E 104 (2021), 034406.
[83] MJ Razavi, T Zhang, H Chen, Y Li, S Platt, Y Zhao, et al., Radial Structure Scaffolds Convolution Patterns of Developing Cerebral Cortex, Front Comput Neurosci 11 (2017) 76.
[84] T Zhang, MJ Razavi, X Li, H Chen, T Liu, X. Wang, Mechanism of Consistent Gyrus Formation: an Experimental and Computational Study, Sci. Rep. 6 (2016) 37272.
[85] MJ Razavi, T Zhang, T Liu, X. Wang, Cortical Folding Pattern and its Consistency Induced by Biological Growth, Scientific Reports. 5 (2015), https://doi.org/10.1038/srep14477.
[86] T Tallinen, JY Chung, JS Biggins, L. Mahadevan, Gyrification from constrained cortical expansion, Proc. Natl. Acad. Sci. 111 (2014) 12667–12672.
[87] S Budday, C Raybaud, E. Kuhl, A mechanical model predicts morphological abnormalities in the developing human brain, Sci. Rep. 4 (2015) 5644.
[88] E. Pannese, Neurocytology: fine structure of neurons, nerve processes, and neuroglial cells. 2., fully revised and updated ed, Springer, Cham, 2015.
[89] P Chavoshnejad, X Li, S Zhang, W Dai, L Vasung, T Liu, et al., Role of Axonal Fibers in the Cortical Folding Patterns: A Tale of Variability and Regularity, Brain Multiphysics (2021), 100029. :.
[90] HT Garimella, RR Menghani, JI Gerber, S Sridhar, RH. Kraft, Embedded Finite Elements for Modeling Axonal Injury, Ann. Biomed. Eng. 47 (2019) 1889–1907.
[91] A Shafiee, M Taghi Ahmadian, M Hoviattalab, Mechanical Characterization of Brain Tissue in Compression, In International Design Engineering Technical Conferences and Computers and Information in Engineering Conference 50138 (p. V003T11A001) (2016), https://doi.org/10.1115/DETC2016-59019 https://doi.org/.